

Effect of surfactant on structural and optical properties of V₂O₅ nanocrystals as a potential catalyst for photodegradation

F. M. Sanakousar^a, C. C. Vidyasagar^{a*}, Swapna. S. Chigari^a, Victor M. Jiménez-Pérez^b, C. C. Viswanath^c, K. Prakash^d, M. B. Sridhara^a

a) Department of PG Studies and Research in Chemistry, Rani Channamma University, Belagavi-591156 Karnataka, India.

b) Universidad Autónoma de Nuevo León, Facultad de Ciencias Químicas, Ciudad Universitaria, Av. Universidad s/n. C. P. 66451, Nuevo León, México.

c) Department of Chemistry, J.S.S Arts, Science & Commerce College, Gokak-591307, India

d) Department of Environmental Science, Gulbarga University, Kalaburgi-585106, Karnataka, India.

Received 17 November 2022; received in revised form 16 January 2023; accepted 10 February 2023 (DOI:10.30495/IJC.2023.1973011.1975)

ABSTRACT

An anionic, cationic, and non-ionic surfactant-assisted wet chemical method was used to synthesize vanadium pentoxide (V₂O₅) nanocrystals. XRD, FESEM, EDX, FTIR, UV-Vis, and PL techniques were used to characterize the V₂O₅ nanocrystals. The formation of V₂O₅ nanocrystals is confirmed by the experimental results. The addition of surfactants had a significant effect on the morphology, crystallinity, and optoelectronic characteristics of the prepared photocatalysts, as per the detailed characterization and analysis of the pertaining light-matter interactions. Additionally, the Scherrer and William-Hall plot methods were used to determine the crystallite sizes from the broadening of the XRD peak. Surfactant addition caused the sample bandgap to broaden, resulting in the blue shift in the distinctive absorption peak of V₂O₅ nanocrystals. To effectively separate the charge carriers during photocatalysis, the most effective photocatalyst (pure V₂O₅) material showed small crystallite size and short migration routes for the charge carriers which is confirmed by XRD and PL analysis. Pure V₂O₅ nanocrystals showed excellent yields in the photocatalytic degradation of Methylene Blue (MB) dye when exposed to sunlight compared to surfactant-assisted V₂O₅. The V₂O₅ catalyst's photostability and reusability were also assessed; after four cycles of testing, the percentage degradation of MB was 94.75%. As per the scavenger experiment, photo-generated holes (h⁺) and superoxide radical's anions (O₂^{•-}) are the major species responsible for the degradation of MB dye. There is a suggested mechanism for the higher degradation efficiency of V₂O₅ at neutral pH when exposed to sunlight. Pure V₂O₅ is a promising and effective photo-catalyst for the photocatalytic degradation of MB dye due to its extremely high performance.

Keywords: Dye degradation, Photocatalysis, Surfactant, Vanadium pentoxide, Wet-chemical method.

1. Introduction

The issues facing people shortly are expected to be access to clean drinking water and a healthy environment [1]. Due to wastewater and other contaminants, the entire globe is experiencing severe environmental crises that are causing numerous deadly diseases [2]. Water contamination from pollutants like heavy metals and organic compounds is now a worldwide issue and is raising a growing number of

concerns [3]. An important source of environmental pollution is dye pollutants from the textile industries. Currently, there are over 10,000 commercially accessible dyes, and further than 7×10⁵ tonnes of dyes wastes are produced each year in the world [4]. However, around 12 % of these dyes are discharged as waste during the dyeing process, and about 20% of this waste is released into the environment [5,6]. A significant cause of eutrophication, aesthetic pollution, and disruptions in aquatic life, these colorful waste waters are released into the ecosystem [7]. MB has been extensively used in the production of dye paper and office supplies, the toning of the color of silk and wool, and other therapeutic and diagnostic processes in both

*Corresponding author:

E-mail address: vidya.891@gmail.com (C. C. Vidyasagar)

human and animal medicine. It possesses a very stable aromatic structure that is complex, hydrophilic, chemically, thermally, and optically stable. As a result, it is difficult to degrade using conventional methods, and releasing MB-contained effluents might seriously harm the environment. The MB-effluents' water pollution causes harmful side effects that include disorientation, nausea, diarrhea, increased sweating, and restless breathing. Due to these issues, environmental research has taken a special interest in developing efficient and cost-effective methods for the complete treatment of waste-water-containing dyes [8–10]. Thus, it is critical for the environment that dyes in aqueous systems are effectively removed [11]. Intense research has been done on the photocatalytic degradation of dyes as well as other organic pollutants, notably in the last decade of the 20th century [12,13]. Large dyes are oxidized into smaller molecules, including water, carbon dioxide, and other mineral by-products, during the dye degradation process. Different traditional chemical, physical and biological techniques were employed to degrade wastewater, however, they are unsuccessful in removing persistent contaminants. To solve this crisis, scientists have been focusing a lot of attention recently on the oxidation process, specifically the advanced oxidation process (AOP), which treats wastewater contaminants [14].

AOP involves the oxidation as well as degradation of organic contaminants by the formation of extremely reactive free radicals in a short time [15]. The photocatalytic activity is accomplished in the existence of a semiconducting catalyst that absorbs an appropriate portion of the solar spectrum to produce reactive oxygen species that cause targets to mineralize. Because of their various benefits, such as improved light absorption capabilities and a long lifespan of photo-generated charge carriers, these photocatalysts are employed in AOPs. The appropriate photocatalysts must be chosen for the AOPs to successfully catalyze the redox processes that occur on their surface when exposed to light. Good photocatalysts are expected to have characteristics like low charge recombination rate so that the catalytic processes will last for a long time (this is also known as the photo-generated charges necessitating to have a long lifetime), responsiveness in visible-light regions so that a free and naturally readily available source of sunlight can be used, easier availability, and being economically inexpensive for widening application [16].

The basic and technological aspects of transition metal oxides were the focus of research in recent years. Metal oxides such as ZnO, TiO₂, WO₃, SnO₂, ZnS, and a variety of other metal oxides have also been studied for

photocatalytic dye degradation [14,17]. V₂O₅, an n-type metal oxide, due to a low bandgap (about 2.4–2.8 eV) is a visible light active photocatalyst and is one of the profound nanocrystal candidates among various oxides studied in the literature. V₂O₅ was chosen as the base material for this study because it has excellent photostability, chemical stability is non-toxic, and may absorb visible light very effectively [16].

Depending on the metal's oxidation state, vanadium may form a wide variety of compounds with oxygen. These oxides have intriguing electrical, optical, magnetic, electrochemical, and structural characteristics which make them suitable for a variety of catalytic applications. The four most common names are mentioned as follows: vanadium (I) oxide (VO), vanadium (III) oxide (V₂O₃), vanadium (IV) oxide (VO₂), and vanadium (V) oxide (V₂O₅). Among the several vanadium oxide compositions, vanadium pentoxide (V₂O₅) is one of the more extensively studied phases, keeping a special set of characteristics such as a small band gap in the range of 2.6 eV. In several articles, vanadium pentoxide (V₂O₅) was employed under UV, visible, and sunlight due to its photocatalytic features [18].

The purpose of the present study is to synthesize environmentally friendly, economically viable, and porous materials for the photocatalytic degradation of dyes. In this study, the influence of several surfactant types such as anionic, cationic, and non-ionic (SDS, TEOA, and Triton-X 100), on the formation of V₂O₅ nanocrystals and their photocatalytic activity was examined. The catalysts were analyzed using XRD, SEM, EDX, IR, UV-Vis, and PL characterization techniques to evaluate their morphology, composition, and optical properties. The photocatalytic activity of prepared V₂O₅ catalysts was tested by MB dye degradation under sunlight irradiation. Furthermore, even after being used repeatedly for the same photocatalytic degradation process, the recycled V₂O₅ catalyst acquired strong stability and durability. In this work, the degradation mechanism of the MB dye degradation by the V₂O₅ catalyst is also studied.

2. Experimental

2.1 Materials and Methods

Ammonium metavanadate, oxalic acid, hydrochloric acid, sodium dodecyl sulfate (SDS), Triton-X 100, triethanolamine (TEOA), Methylene Blue (MB), p-benzoquinone (p-BQ), isopropyl alcohol (IPA), silver nitrate (AgNO₃) and sodium oxalate (SO) were all procured from Merk. All of the chemicals were of analytical grade and utilized without further

purification. Throughout the study, double-distilled water was used.

2.2 Synthesis of V_2O_5

A feasible wet chemistry procedure was used to synthesize the photocatalyst (**Scheme 1**). In a typical preparation, 3.4 g ammonium metavanadate was dissolved in the water in addition to the proper amounts of SDS, Triton-X 100, and TEOA surfactants. The pH of the solution was set at 2 by adding 1.12 g oxalic acid to it, resulting in a yellowish solution. After a few minutes of stirring, HCl (10 drops) was dropwise added to the resulting solution, turning it green then kept at 180 °C since it stirred for 24 hours. After cooling, the catalysts were filtered out of the solution and washed again with water and ethanol. To thoroughly remove the surfactants from the synthesized materials, the samples were calcined at 750 °C for 2 hours (ramp rate of 5 °C/min), then elevated to 750 °C for an additional two hours. The samples will now be labeled by the names of the surfactants: pure V_2O_5 (without surfactant), V_2O_5 -SDS, V_2O_5 -TEOA, and V_2O_5 -Triton X 100 [19].

2.3 Material Characterization

An X-Ray diffractometer (BRUKER: D8 advance) linked with Cu-K radiation at $\lambda=0.154$ nm and Cu-K at $\lambda=0.13922$ nm in the range of two values 10-80° was used to examine the synthesized nanocrystals for their crystalline nature. The surface morphology and size distribution of the samples were investigated using a Carl Zeiss AG-ULTRA 55 field emission scanning electron microscope (FE-SEM) (200KV) with energy-dispersive X-ray spectroscopy (EDAX). The IR spectra of KBr pellets were recorded using a spectrophotometer of the Perkin Elmer spectra RX-1 model. Using a UV-Vis spectrophotometer, model SB 4000, made by Ocean

Optics, U.S.A, the optical absorbance and photo response of V_2O_5 nanocrystals were assessed.

2.4 Photocatalytic Degradation Experiment

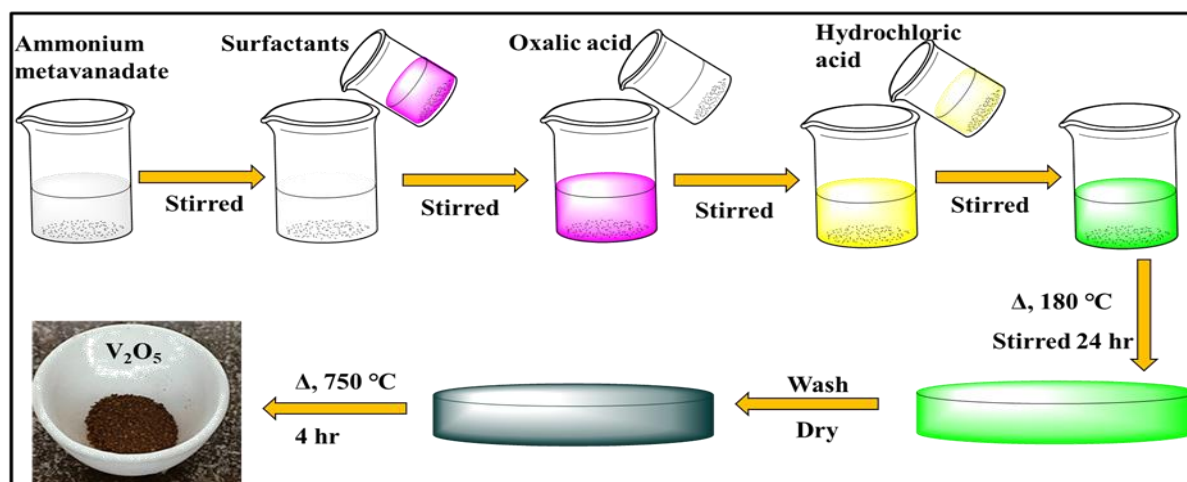
The photocatalytic degradation of methylene blue (MB) was examined to determine the effect of surfactants on the activity of V_2O_5 photocatalysts. In a brief, 50 mL, 10 ppm (0.01 g /L) of MB aqueous solution was stirred in a magnetic stirrer to disperse 0.01 g of the synthesized catalyst at natural pH in the dark until the adsorption-desorption equilibrium was reached before the light illumination. The photocatalytic studies were then performed as exposed to sunlight at time intervals of 0 to 30 mins. The catalyst was removed from the suspension under centrifugation at regular intervals, and 4 mL of the supernatant solution was taken to measure the absorbance at 664 nm and determine the kinetics of the pollutant's degradation with a UV-vis spectrophotometer [18, 20].

By using the following equation, degradation efficiency was determined:

$$\text{Degradation efficiency (\%)} = (C_0 - C) / (C_0) * 100 \quad (1)$$

C_0 and C are the concentrations of the solution at time $t=0$ before and time t , after the irradiation, respectively [18,20].

To understand the mechanism and identify the reactive species in the photodegradation processes, photocatalytic degradation tests were performed with the addition of scavengers. p-benzoquinone (p-BQ), isopropyl alcohol (IPA), silver nitrate ($AgNO_3$), and sodium oxalate (SO) were utilized specifically as, superoxide radicals, hydroxyl radicals, electrons, and holes scavengers, respectively [16]. Additionally, the stability and reusability of the photocatalyst can be examined by repeating 4 cycles.



Scheme 1. Surfactant-assisted wet chemistry method for the preparation of V_2O_5 and pure V_2O_5 (without adding a surfactant to ammonium metavanadate).

3. Results and Discussion

3.1 Structural Analysis (XRD)

One of the most widely used techniques for characterizing nanocrystals is X-Ray diffraction (XRD). The structure, type of material, approximate number of elements, and crystallographic characteristics of prepared catalysts were studied using the XRD Analysis. Fig. 1 shows the XRD patterns of the V_2O_5 , V_2O_5 -SDS, V_2O_5 -TEOA, and V_2O_5 -Triton-X 100, surfactants. The orthorhombic α - V_2O_5 (JCPDS card no.041-1426) phase is visible in the XRD pattern for the synthesized pure V_2O_5 (**Fig. 1a**), and there are no other phases of peaks, showing the high purity of the V_2O_5 phase [21]. The monoclinic phase of V_2O_5 is seen in the XRD pattern for the V_2O_5 -SDS as-synthesized (**Fig. 1b**) (ICDD-98-003-1428) [22]. The XRD pattern of V_2O_5 -TEOA is displayed in Fig. 1c. As per **Fig. 1c** V_2O_5 was responsible for the XRD plane at 2 theta values of 27.79° (110), 33.30° (101), 36.86° (130), 40.01° (002), 42.20° (012), 44.68° (141), 45.40° (060) and 53.00° (102) [23]. **Fig. 1d** displays the XRD spectra of V_2O_5 -Triton X 100. The main peaks of diffraction are related to the orthorhombic crystal structure of V_2O_5 and are located at 2 theta = 14.57°, 19.45°, 25.39°, 30.13°, and 33.79°, respectively (JCPDS 41-1426) [24].

Scherrer's equation was used to calculate the average crystallite size D of the particles by the XRD line broadening measurement.

$$(D)=0.9\lambda/(\beta \cos \theta) \quad (2)$$

Where D is the average crystalline size, λ is the wavelength of the X-ray used (Cu-Ka 1.5406 Å), θ is Bragg's diffraction angle in radians, and β is the Full width at half maxima in radians.

The average crystalline sizes of the pure V_2O_5 , V_2O_5 -SDS, V_2O_5 -TEOA, and V_2O_5 -Triton-X 100 nanocrystals were calculated to be around 22.71, 35.25, 36.33, and 42.71 nm, respectively [25,26].

The Scherrer equation is often only suitable for crystal grain sizes less than 100 nm. Additionally, when mechanical force is applied to a crystal to prepare a composite, the crystal is placed under some strain, which changes the d -spacing. These d variations lead to the fluctuation according to Bragg's law ($n\lambda = 2d \sin\theta$). In such cases, the Williamson-Hall (W-H) equation is a superior method, to evaluate grain size and the simplest model to examine the relationship between crystallite size and strain. The W-H equation was used to study the effects of size and strain broadening on the crystallite size concurrently [1,25,27,28].

The lattices strain and crystalline size of each sample were determined using the William-hall equation as shown by equation (3):

$$\beta \cos \theta = \frac{0.9\lambda}{D_{WH}} + 4\varepsilon \sin \theta \quad (3)$$

$$\text{Micro-strain } (\varepsilon) = \beta \cos \theta / 4 \quad (4)$$

$$\text{Dislocation density } (\delta) = 1/D^2 \quad (5)$$

Where θ is Bragg's diffraction angle, ε is the strain, β is the FWHM (in radians) and D_{WH} is the average crystalline size [29] [30].

As seen in equation (3), the first term in the right hand of this equation verifies the Scherrer equation, while the second term illustrates the effect of internal strain (or Stokes and Wilson expression). Commonly, the size of the crystallite, strain, instrumental parameters and crystal defects may affect the β -value. When strain broadening is independent of $1/d$, a rise in $1/d$ value enhances the effect of the strain broadening. Additionally, the W-H equation might lead to the net Scherrer equations when the strain factor ε is close to zero. Both effects are more frequently present, hence the W-H equation must be used to analyze both simultaneous effects.

Fig. 2a-d illustrates a typical W-H plot for the nanocrystals, which was constructed by plotting the data for $\beta \cos\theta$ versus $4 \sin\theta$. The result was a linear curve with the intercept ($k\lambda/d$) and slope (ε). A positive slope was observed in this case, confirming the presence of tensile strain in the sample. The grain boundary, contact and coherency stresses, triple junction, and stacking faults all cause this tensile strain. The positions of the diffraction peaks could also change relatively as a result of these factors. The crystallite size of the nanocrystals was determined by the intercept values of the W-H plots to be about 25.90, 53.30, 56.11, and 114.54 nm for the as-prepared pure V_2O_5 , V_2O_5 -SDS, V_2O_5 -TEOA, and V_2O_5 -Triton-X 100 nanocrystals, respectively. The results demonstrate various crystallite sizes calculated using the Scherrer and W-H equations, confirming the effects of crystallite size and strain on the peak broadening for the samples [1,25,27,28].

Table 1 provides a summary of the calculated crystallite sizes, microstrain, and dislocation density. **Table 1** shows that the addition of various surfactants increases the crystallite size, as determined by the Scherrer and William-Hall plot methods.

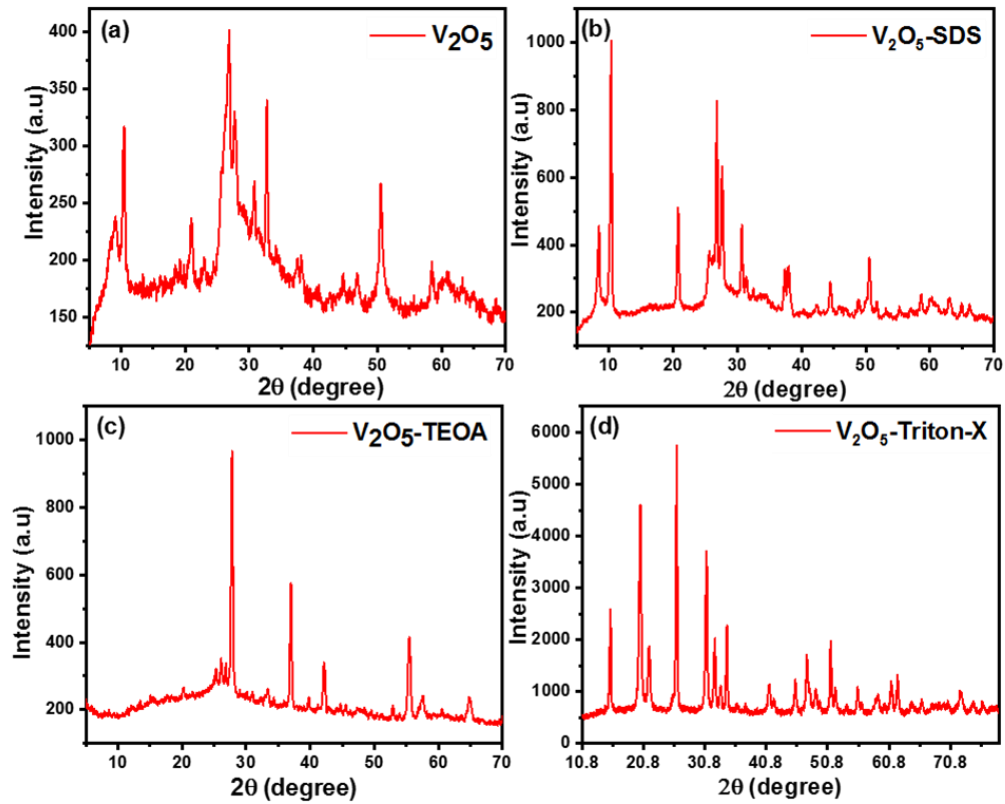


Fig. 1. XRD patterns of (a) pure V_2O_5 , (b) V_2O_5 -SDS, (c) V_2O_5 -TEOA, and (d) V_2O_5 -Triton-X 100 nanocrystals.

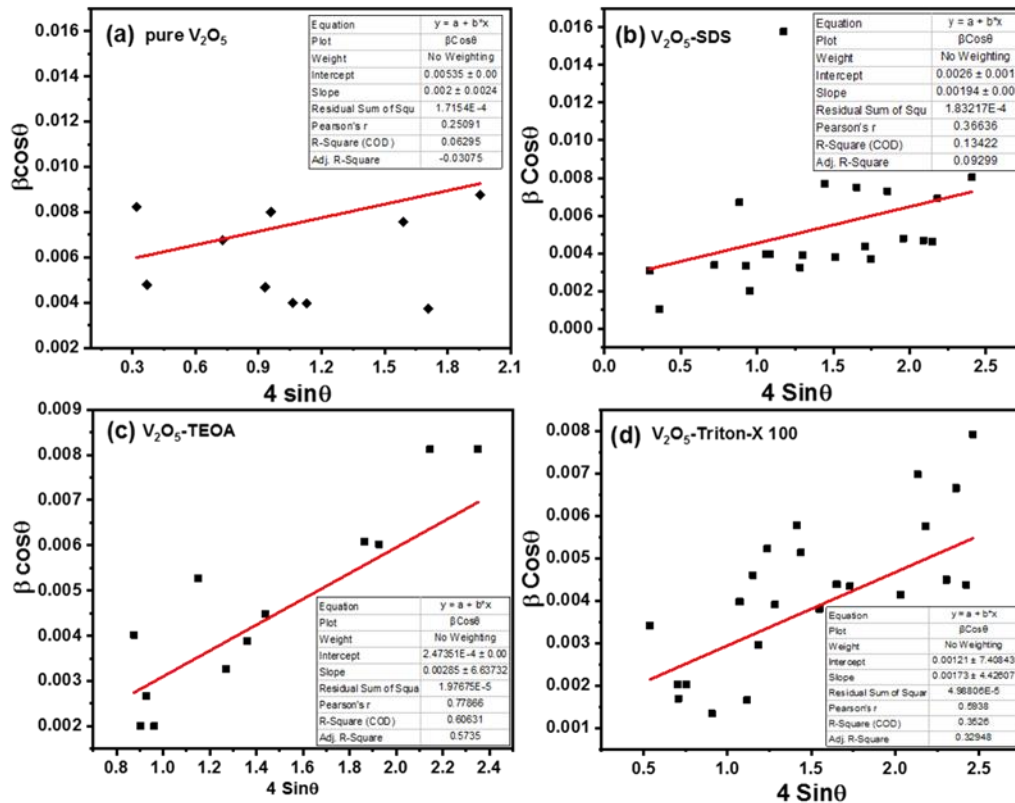


Fig. 2. Williamson hall plot of (a) pure V_2O_5 , (b) V_2O_5 -SDS, (c) V_2O_5 -TEOA, and (d) V_2O_5 -Triton-X 100 nanocrystals. The William-hall method provides a straight line with the intercept ($\frac{0.9\lambda}{D_{WH}}$) equal to the crystalline size and a slope (ϵ) equal to the micro-strain in the plot of $\beta \cos\theta$ versus $4 \sin\theta$.

Table 1. Crystallite size, micro-strain, and dislocation density values of pure V₂O₅ and surfactant-assisted V₂O₅ nanocrystals.

Samples of surfactant-assisted V ₂ O ₅	Debye- Scherrer method			Williamson-Hall method		
	Crystallite size (nm)	Micro-strain (ϵ) x10 ⁻³	Dislocation density (δ) x10 ⁻³	Crystallite size (nm)	Micro-strain (ϵ) x10 ⁻³	Dislocation density (δ) x10 ⁻³
Pure V ₂ O ₅	22.71	8.52	3.804	25.90	2	1.490
V ₂ O ₅ -SDS	35.25	4.203	1.973	53.30	1.94	0.352
V ₂ O ₅ -TEOA	36.33	3.039	1.278	56.11	2.85	0.317
V ₂ O ₅ -Triton X 100	42.71	2.646	0.945	114.54	1.73	0.076

3.2 Morphological Analysis (FE-SEM and EDX)

The field emission scanning electronic microscope (FE-SEM) was carried out to know information about the morphology of the prepared samples. The morphological images of the as-synthesized V₂O₅ nanocrystals with various surfactants are displayed in **Fig. 3a-d**. A large surface area of the samples with irregular morphology at a range of 32-53 nm is shown on the pure V₂O₅ in **Fig. 3a** [31]. For the V₂O₅-SDS sample, **Fig. 3b** depicts the existence of rod-like nanostructures covered in large nanosheets. Finally, it was found that an irregular structure with an incredibly smooth surface had formed, showing that the V₂O₅ particles had appeared as nanoflakes at a size between 66 to 70 nm [32]. The V₂O₅-TEOA samples resemble fibers, and the pores seem to be formed by aggregates of particles with irregular morphology as depicted in **Fig. 3c** in a size range of 17-26 nm [4] and **Fig. 3d** depicts the V₂O₅-Triton-X 100 sample's irregular cubic morphology at a range between 72 to 74 nm [19].

The results imply that the V₂O₅ nanocrystals prepared by different surfactants showed different morphology and pure V₂O₅ nanocrystals showed mesoporous, crystalline, and rough surface area. In general, rough surfaces are more photo-catalytically active than smooth surfaces. These micropores are sufficient to affect the photocatalytic activity of pure V₂O₅ nanocrystals because a rough surface will exhibit a greater surface area, resulting in more photocatalytic sites.

From **Fig. 4** the elemental chemical composition is qualitative and quantitative, the energy dispersive X-Ray (EDX) spectroscopy was used, which clearly shows that the nanocrystals contain the elements Vanadium and Oxygen as predictable and that the chemical purity is achieved.

3.3 FTIR Analysis

Surfactant molecule absorption at the V₂O₅ surface is studied using Fourier Transform Infrared Spectroscopy. **Fig. 5** displays the FTIR spectra of V₂O₅ samples synthesized with various surfactants in the wavenumber ranges of 4000 cm⁻¹ to 400 cm⁻¹ for functional groups and chemical bonds. Functional groups and fingerprint regions combine to form the FTIR spectrum. Oxides produce fingerprint-region absorption bands. Asymmetric V=O and V-O-V (bridge oxygen) vibrations were seen in the vibrational bands at 1101.4 cm⁻¹ and 985 cm⁻¹ and asymmetric and symmetric V=O bond characteristic bands were obtained at 617 cm⁻¹ and 477 cm⁻¹, respectively, for all V₂O₅ nanocrystals (**Fig. 5**). The bending vibrations of carbonyl is responsible for the absorption peak at 1633.94 cm⁻¹. O-H stretching is linked to the formation of the FTIR band at wave number (3400 cm⁻¹). Changes in the surfactants reduced the band's intensity. This shows the direct relationship between the different surfactants and bonds. [33, 34]. The data obtained demonstrate the presence of V-O (vibrational mode), carbonyl, and the O-H groups, similar results have been found in the literature [1].

3.4 Optical Analysis

3.4.1 UV-Visible Spectral Analysis

In the literature, it has been shown that the Kubelka-Munk model and Tauc plots are superior and more accurate ways to estimate the band gap energy of semiconducting materials. **Fig. 6** shows the surfactant-dependent absorbance in UV-vis optical properties in the range of (200-800 nm) by changing the surfactants (SDS, Triton X 100, TEOA). The V₂O₅ as-synthesized sample's absorption peaks may be seen to occur around (3.50 eV). Surfactant addition caused the bandgap of the samples to broaden, which resulted in the blue shift in the distinctive absorption peak of V₂O₅ nanocrystals.

The optical band gap (E_g) was calculated by plotting the graph from the following equation (known as the Tauc plot).

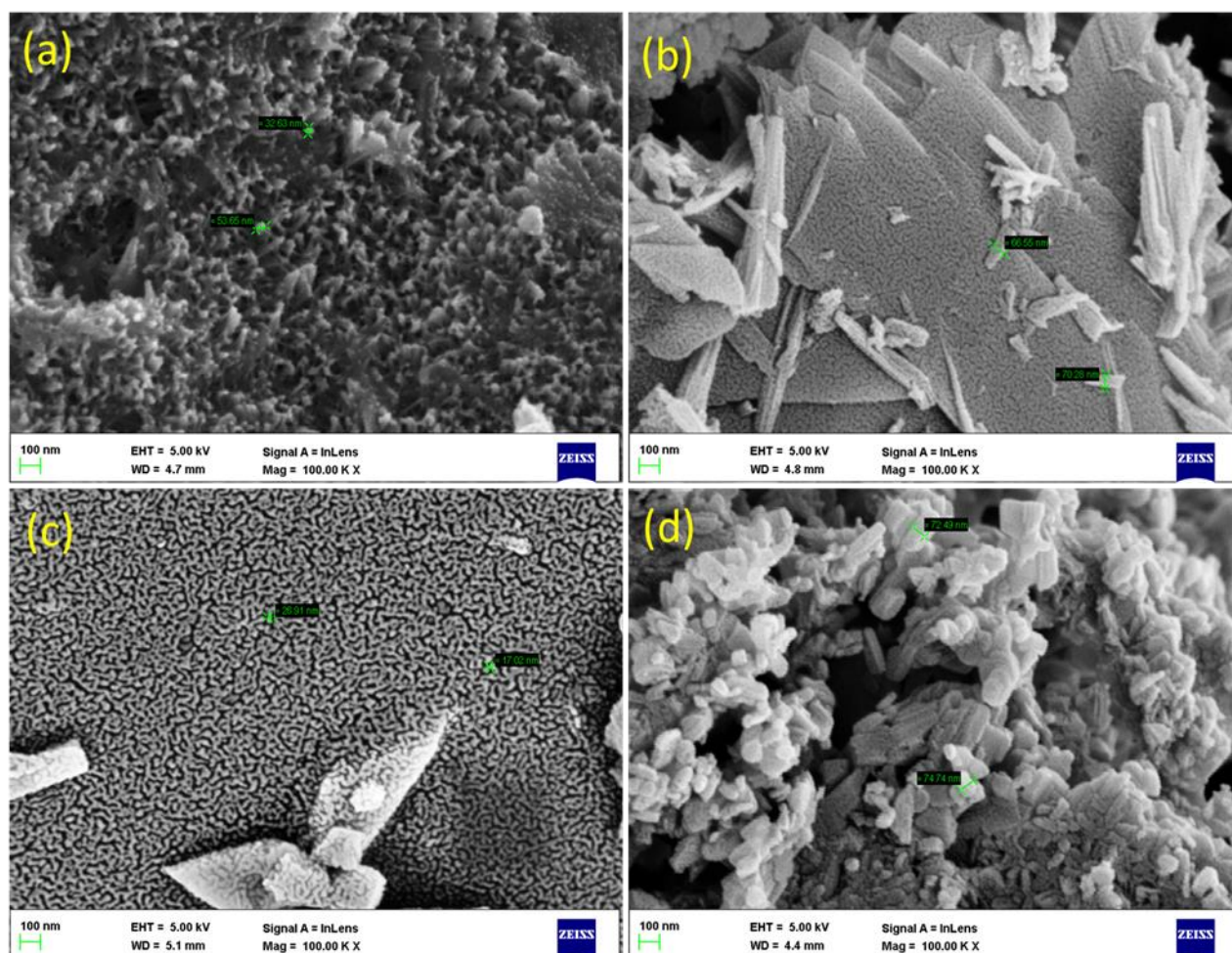


Fig. 3. FESEM images of (a) pure V_2O_5 , (b) V_2O_5 -SDS, (c) V_2O_5 -TEOA, and (d) V_2O_5 -Triton-X 100 nanocrystals.

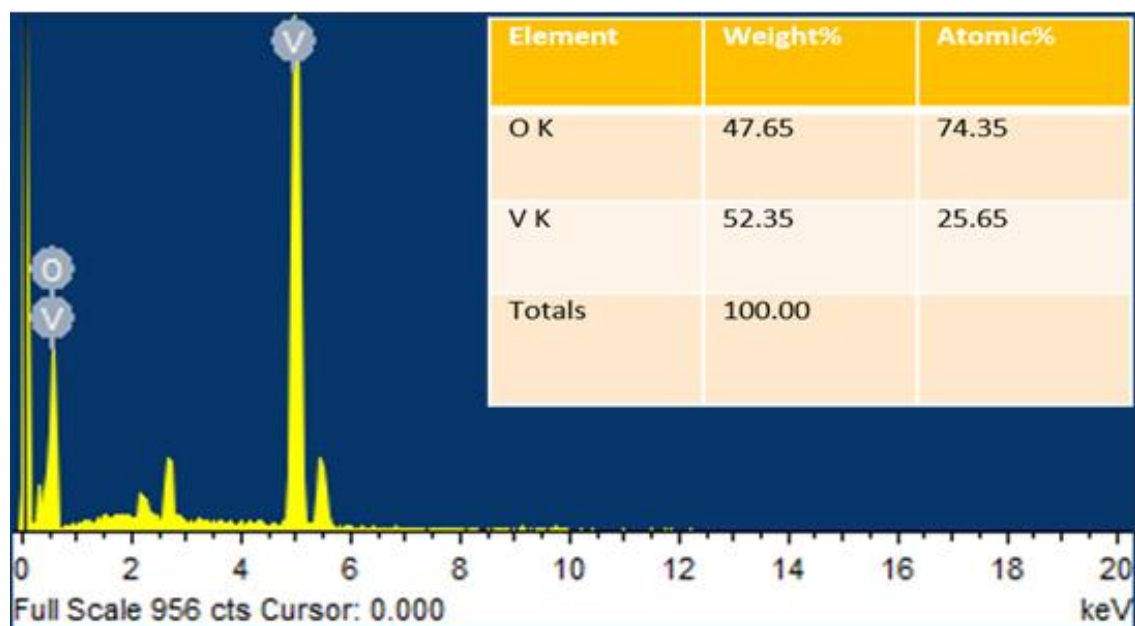


Fig. 4. EDX image of pure V_2O_5 nanocrystals.

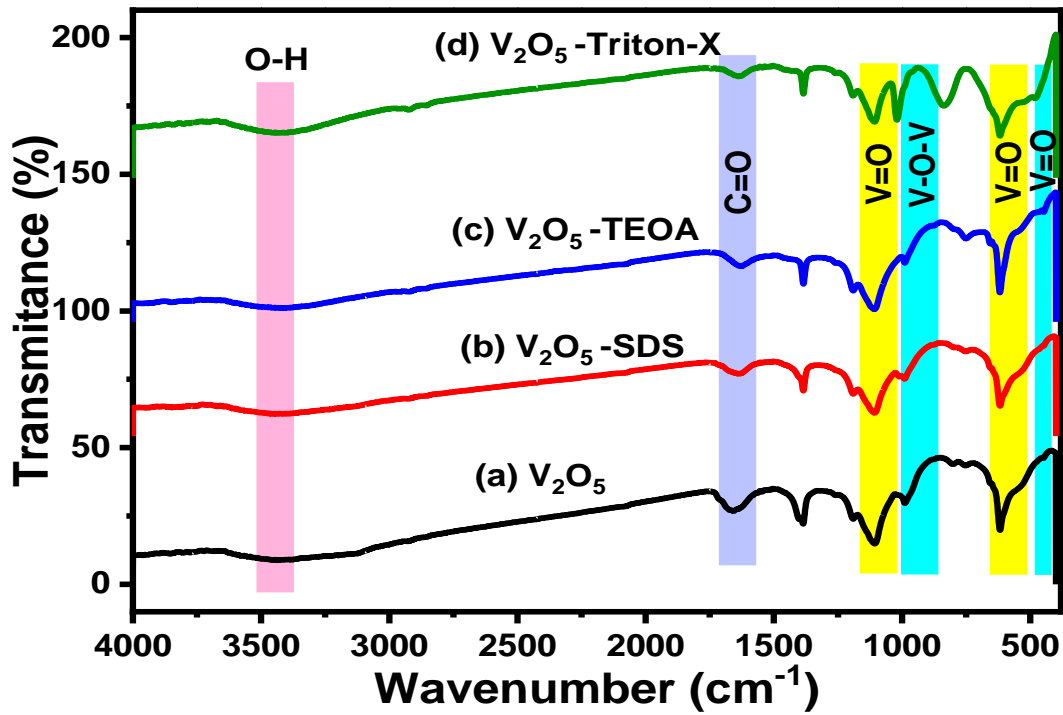


Fig. 5. FTIR spectra of (a) pure V₂O₅, (b) V₂O₅-SDS, (c) V₂O₅-TEOA, and (d) V₂O₅- TritonX 100 nanocrystals.

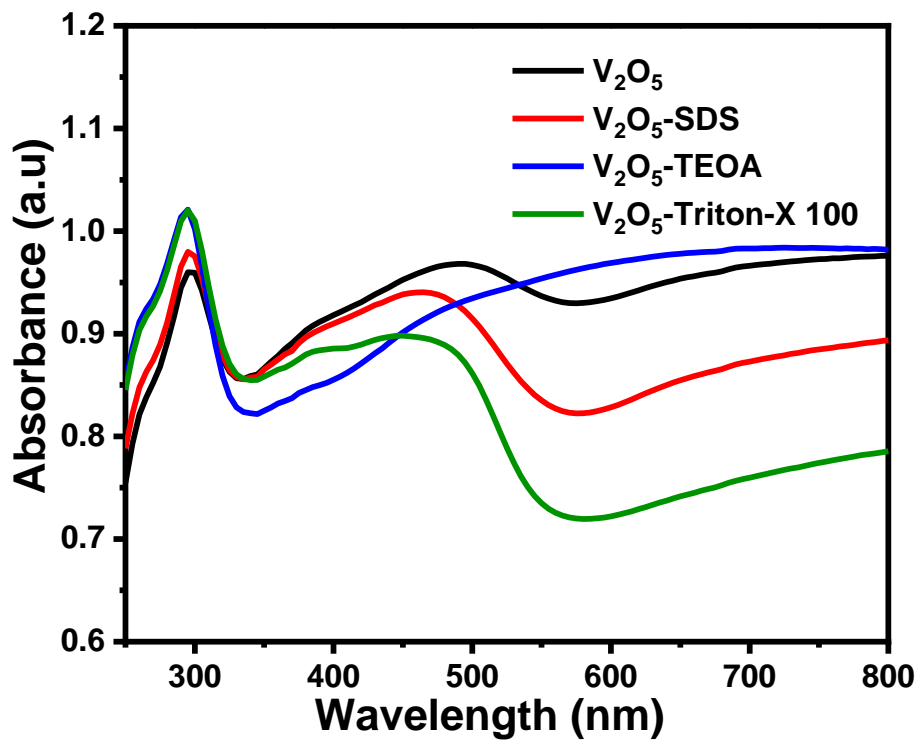


Fig. 6. UV-Visible absorbance spectra of the prepared, pure V₂O₅, V₂O₅-SDS, V₂O₅-TEOA, and V₂O₅- Triton-X 100 nanocrystals.

$$(\alpha h\nu) = (h\nu - E_g)^n \quad (6)$$

The plot of $(\alpha h\nu)^{1/n}$ versus $h\nu$ (the photo energy) is shown in a typical Tauc plot. Where h is the plank's constant, n is an integer, ν is the frequency of the incident light, and E_g is the material's band gap. For the various transition levels of direct and indirect allowed, direct and indirect forbidden interactions with photons, an integer n can have the values $1/2$, 2 , $3/2$, and 3 . The value of E_g may be obtained using the graph of $(\alpha h\nu)^{1/n}$ versus $(h\nu)$ and projecting the straight line fitted to the graph to the x-axis, where the quantity $(\alpha h\nu)^{1/n} = 0$ [35–37]. The results of the above equation with $n=1/2$ assuming the direct allowed transition in V_2O_5 samples are shown in **Fig. 7a-d**'s Tauc plot. The direct transition by the occupied 2p bands of oxygen to the unoccupied 3d bands of vanadium in pure V_2O_5 is credited with causing a band gap of 3.54 eV. When SDS, Triton X

100, and TEOA were added to V_2O_5 , the band gap energy values are obtained to be 3.55 eV, 3.65 eV, and 3.57 eV. The findings suggest that the V_2O_5 nanocrystals synthesized using various surfactants had various band gaps. [22].

3.4.2 PL Analysis

The V_2O_5 nanocrystal's room temperature PL spectra are shown in **Fig. 8**. Increased surface states, which are typically formed in nano-size crystal structures for the reason that they can act as traps and reduce excitonic emission, may be the cause of PL quenching [31]. When surfactants are present in the sample, the structure is rearranged to have longer nano-sizes, which results, in an increase in PL intensity compared to without surfactant (pure V_2O_5). The electron-hole pairs are recombined from the lowest split of the V 3d CBs to the

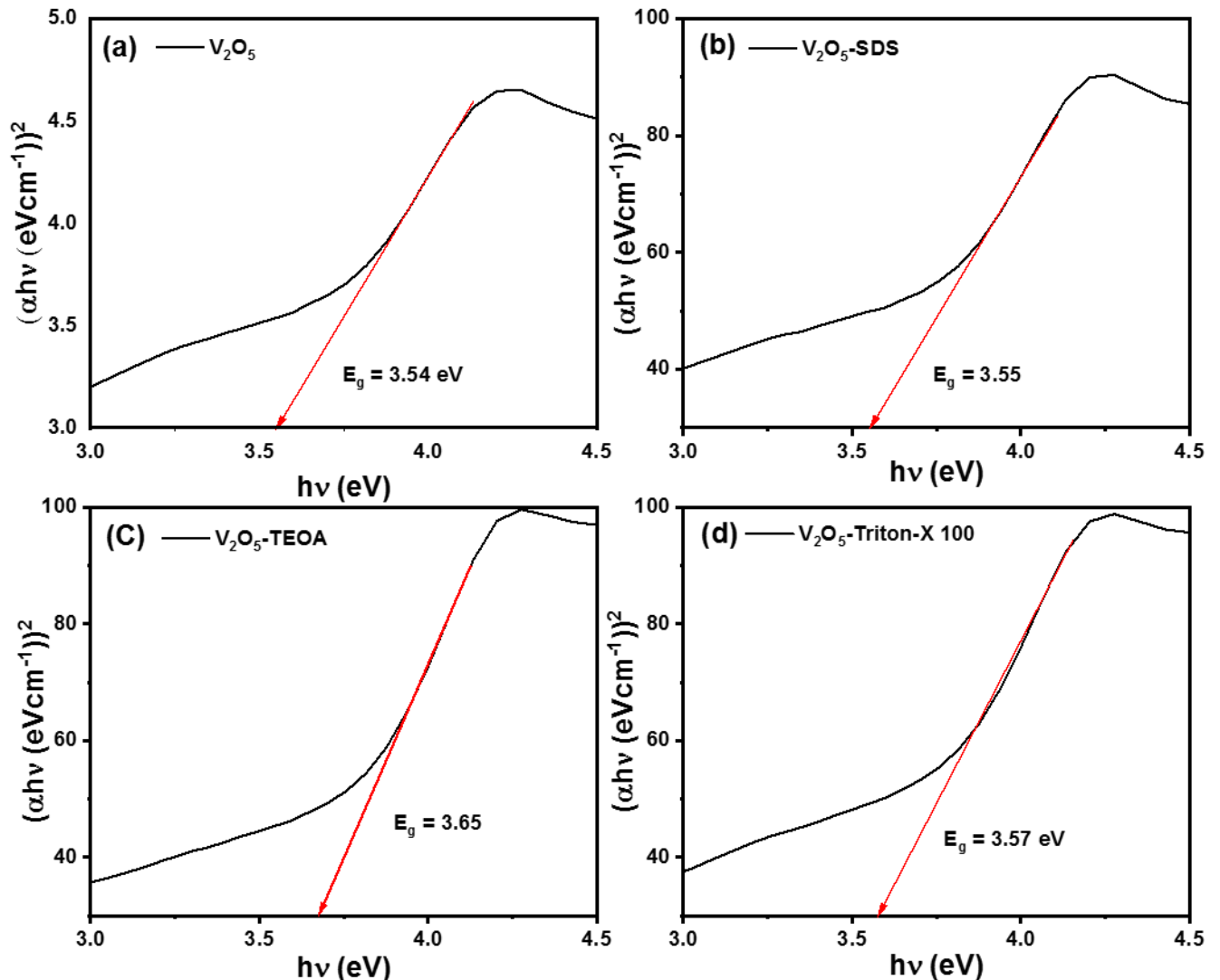


Fig. 7. Tuac plot of (a) pure V_2O_5 , (b) V_2O_5 -SDS, (c) V_2O_5 -TEOA, and (d) V_2O_5 - Triton-X 100 nanocrystals.

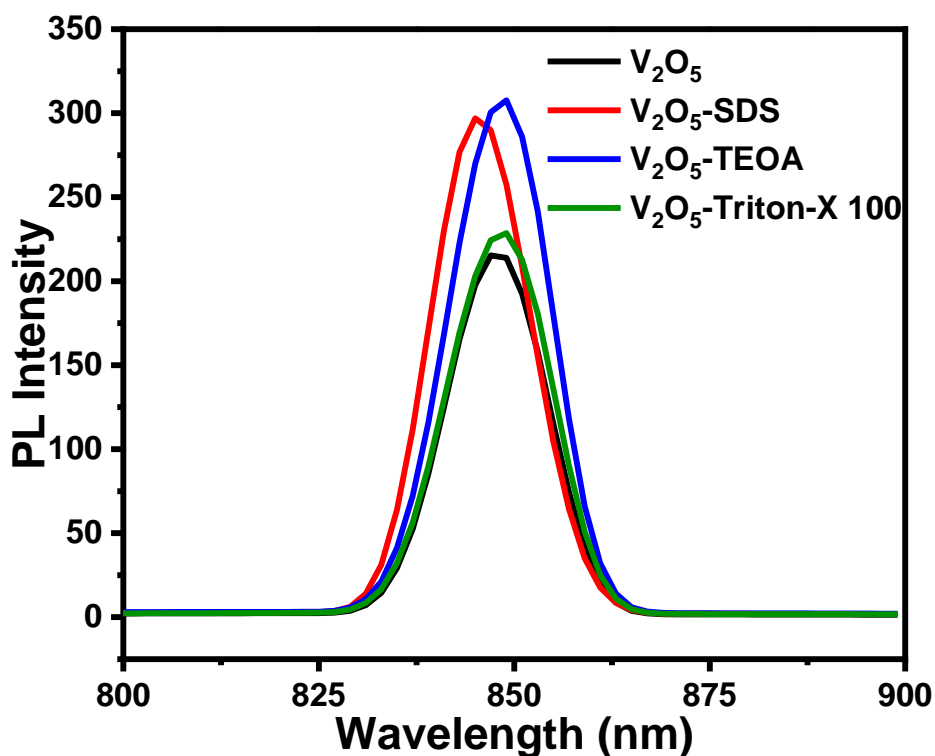


Fig. 8. PL spectra of the prepared, pure V_2O_5 , V_2O_5 -SDS, V_2O_5 -TEOA, and V_2O_5 -Triton-X 100 nanocrystals.

top of the O 2p VBs, which results in intense PL emission at 850 nm. The peak at 850 nm was considerably enhanced, clearly showing how the surfactants affected the V_2O_5 nanocrystal defects. Pure V_2O_5 showed a reduction in PL intensity indicating that photo-induced electron-hole pairs are less able to recombine and that electron-hole migration is increasing [38], resulting in enhanced photocatalytic degradation efficiency.

3.5 Photocatalytic Activity

The photocatalytic activity of synthesized pure V_2O_5 and different surfactant-assisted V_2O_5 nanocrystals was studied using MB dye as a model pollutant in a photocatalytic degradation and kinetic study in 30 mins under sunlight irradiation. In our study, 10 ppm of MB dye solution was taken to analyze the photocatalytic degradation of dye, because more dimer and trimer of MB molecules might be present in the solution at higher MB concentration, and they are responsible for less photodegradation [39,40]. The MB dye's percentage degradation with pure V_2O_5 , V_2O_5 -SDS, V_2O_5 -TEOA, and V_2O_5 -Triton-X 100 nanocrystals as a function of irradiation time are displayed in **Fig. 9a** the results showed that the sample's degradation efficiencies were

in the following order: pure V_2O_5 (94.75%) > V_2O_5 -SDS (80.48%) > V_2O_5 -Triton X 100 (70.43%) > V_2O_5 -TEOA (54.21%). The photodegradation of MB using pure V_2O_5 catalyst is seen in **Fig. 9b** as a reduction in UV-visible absorption spectra. As can be seen, the process that was used to evaluate the extent of MB molecule degradation resulted in a reduction in the intensity of the main peak at 664 nm. Therefore, in all of the aforementioned photodegradation experiments, this reduction in absorbance was utilized to calculate the percentage of degraded MB molecules [40]. **Fig. 9b** shows the changes in the absorption spectra caused by the degradation of 10 ppm MB (0.01 g/L) over 0.01 g photocatalyst composed of pure V_2O_5 at various time intervals ranging from 0-30 mins under sunlight irradiation. The changes in concentration C/C_0 vs time are shown in **Fig. 9c**, as the irradiation time increases there is a decline in the concentration of the dye.

The Langmuir-Hinshelwood (L-H) model is used to explain the photocatalytic reaction kinetics to understand the kinetic parameters of photocatalytic MB dye degradation. The photocatalytic degradation reaction rates were calculated utilizing pseudo-first-order kinetics using the following formula:[41–44]

$$\ln(C_0/C_t) = kt \quad (7)$$

Where k is the pseudo-first-order reaction rate constant (min^{-1}), t is the reaction time, C_0 is the dye's initial concentration, and C_t is the dye concentration at regular intervals of time (t) [45].

The pseudo-first-order kinetics of photocatalytic degradation reactions are shown by the plot of $\ln(C_0/C_t)$ v/s time in **Fig. 9d**. The rate constant (k) was determined by the slope of the plot

of $\ln(C_0/C_t)$ vs response time (t), as shown in **Fig. 9d**. The MB solution's photodegradation follows pseudo-first-order kinetics pure V_2O_5 shows a higher rate of photocatalytic degradation of MB than surfactant-assisted V_2O_5 , with a rate constant and correlation coefficient of $K=0.06901 \text{ min}^{-1}$ ($R^2 = 0.7494$) compared to $K=0.04451 \text{ min}^{-1}$ ($R^2 = 0.7526$) for V_2O_5 -SDS, $K=0.03878 \text{ min}^{-1}$ ($R^2 = 0.9546$) for V_2O_5 -Triton X 100, and $K=0.0264 \text{ min}^{-1}$ ($R^2 = 0.9966$) for V_2O_5 -TEOA. **Fig. 9** shows that only a small percentage of degradation was seen in the catalyst synthesized from SDS, Triton X 100, and TEOA. The 94.75 % degradation was seen in

the case of pure V_2O_5 . Based on these results, MB can be effectively degraded by pure V_2O_5 nanocrystals when compared to the other three samples.

3.5.1 Scavenger Experiment

Scavenger studies are crucial to elucidate the significance of each species (e^- , h^+ , $\text{O}_2^{\bullet-}$, and $\text{OH}^{\bullet-}$) in the degradation process and to predict the photodegradation mechanism. When the mechanism is known, conditions may be optimized more effectively to increase photocatalytic efficiency. In literature, the effects of several scavenging agents like carbonate (HCO_3^-), nitrate (NO_3^-), chloride (Cl^-), and ascorbic acid (AA) were studied on the photodegradation activity of the nanocrystals. Superoxide radicals ($\text{O}_2^{\bullet-}$) can be successfully scavenged by AA, while free electrons (e^-) can be scavenged by nitrate, the resultant $\text{OH}^{\bullet-}$ radicals can be efficiently scavenged by carbonate and bicarbonate species, and the photogenerated holes (h^+) can be scavenged by chloride [39,46]. In our case to better understand the likely active radicals like e^- , h^+ , $\text{O}_2^{\bullet-}$, and $\text{OH}^{\bullet-}$ (silver nitrate (AgNO_3), sodium oxalate

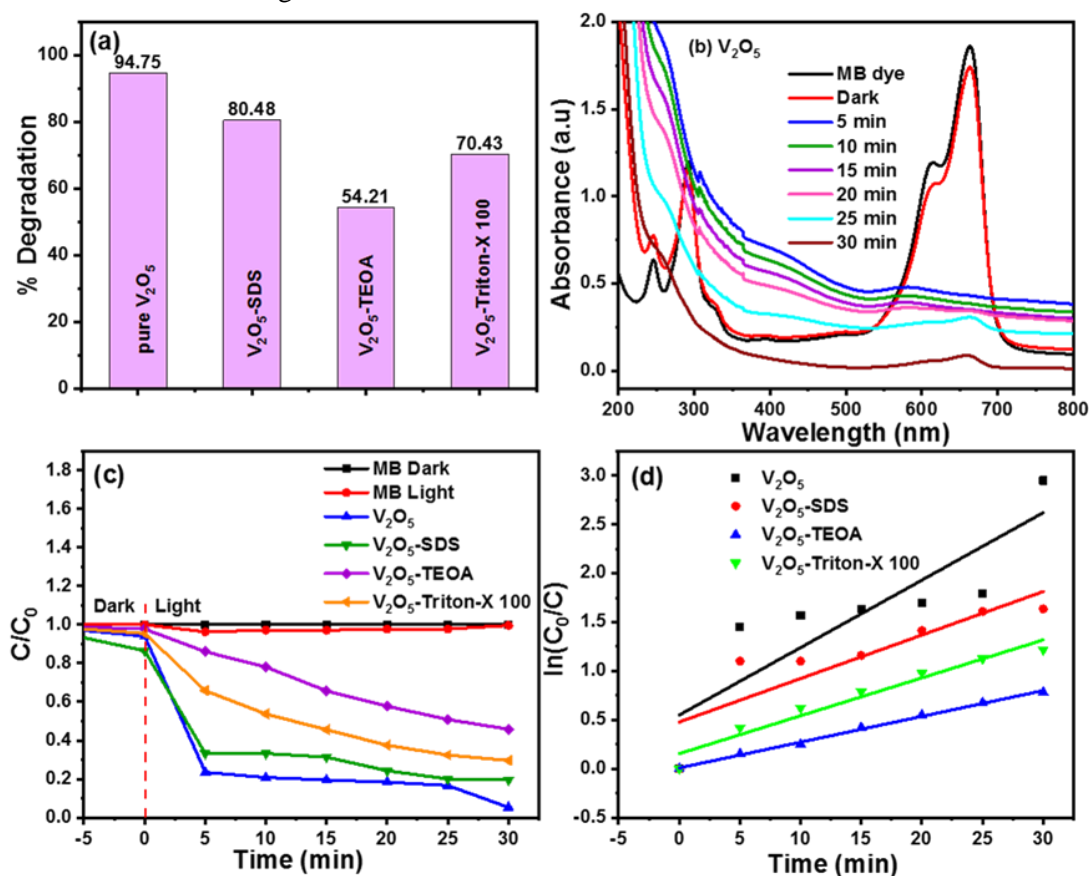


Fig. 9. (a) The plot of the percentage degradation of MB dye using pure V_2O_5 , V_2O_5 -SDS, V_2O_5 -TEOA, and V_2O_5 -Triton-X 100 nanocrystals, (b) Absorbance spectra of pure V_2O_5 , (c) plot of C/C_0 vs time and (d) $\ln C_0/C$ vs time, using V_2O_5 with different surfactants as a function of irradiation time using 0.01 g catalyst, in 10 ppm MB dye solution at natural pH in 30 min sunlight irradiation.

(SO), *p*-Benzoquinone (*p*-BQ), and isopropyl alcohol (IPA)), were used at a concentration of 1 mM, participate in the MB dye degradation during photocatalytic processes, a radical scavenging experiment was carried out. **Fig. 10** displays the percentage degradation data of the photodegradation studies conducted with pure V_2O_5 in the addition of scavenger molecules. The degradation rates of the MB dye are 81.2%, 69.7%, and 38.9% respectively when isopropyl alcohol (IPA), silver nitrate ($AgNO_3$), and *p*-Benzoquinone (*p*-BQ) were added to the reaction solution. In comparison, the degradation is only 20% when sodium oxalate (SO) was utilized. In particular, MB degradation is constrained compared to degradation of dye without scavenger (94.75%), when these trapping molecules were present. Free radicals e^- , h^+ , $O_2^{\bullet-}$, and OH^{\bullet} are typically trapped by scavengers *p*-BQ, $AgNO_3$, SO, and IPA, respectively, resulting in a reduction in degradation. These photodegradation data show that a significant amount of e^- , h^+ , and $O_2^{\bullet-}$ were formed in photoinduced reactions when MB was exposed to sunlight, and they serve to degrade MB dye. However, when SO is used, the degradation is at its lowest (25.3%) indicating that the holes (h^+) and superoxide anion radicals ($O_2^{\bullet-}$) are primarily responsible for the photocatalytic degradation of MB in this instance. The photodegradation of MB is influenced by all radicals, although to various extents.

3.5.2 Mechanism

In a typical photocatalytic mechanism, three steps are taken part: the first layer is dyes diffusion, in which dye molecules transfer from aqueous to the outer surface of the catalyst; the second is inner diffusion, also known as intraparticle diffusion, in which dye molecules are adsorbed to the interior pores of the catalyst; and the third step, in which the dye molecules interact with the internal pore's active sites of the catalyst. **Scheme 2** shows a schematic representation of the photo-assisted degradation phenomena based on the explanation above. A photon with an energy equal to or greater than 3.54 eV interacts with the V_2O_5 nanocrystal photocatalyst to produce an electron-hole pair, where, the electrons are excited to the CB and the holes remain in the VB. The photogenerated CB electrons may move quickly to the V_2O_5 nanocrystals and decrease a part of the V^{5+} ions to V^{4+} , which promotes the separation and transport of the photogenerated electron and hole pairs. Under the influence of the environment, the electrons that the V^{5+} ions have taken are subsequently quickly transferred to oxygen molecules, regenerating the V^{4+} to produce $O_2^{\bullet-}$ superoxide anion radicals. The V^{5+}/V^{4+} redox cycle, as given in the reaction, may be used to define the process. While the hole in the VB interacts with a water molecule (H_2O) to produce hydroxyl radicals [22]. Hydroxyl radicals and superoxide radicals are powerful oxidizing agents that break down organic contaminants into less harmful substances and minerals. The following equations explain the overall reaction phenomenon [47].

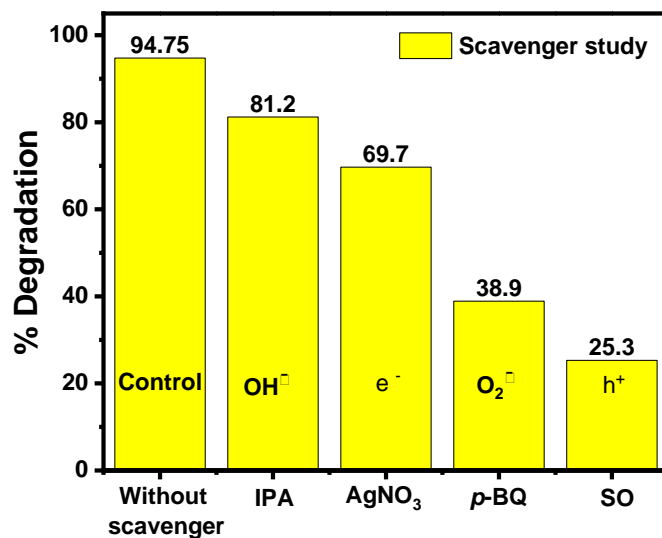
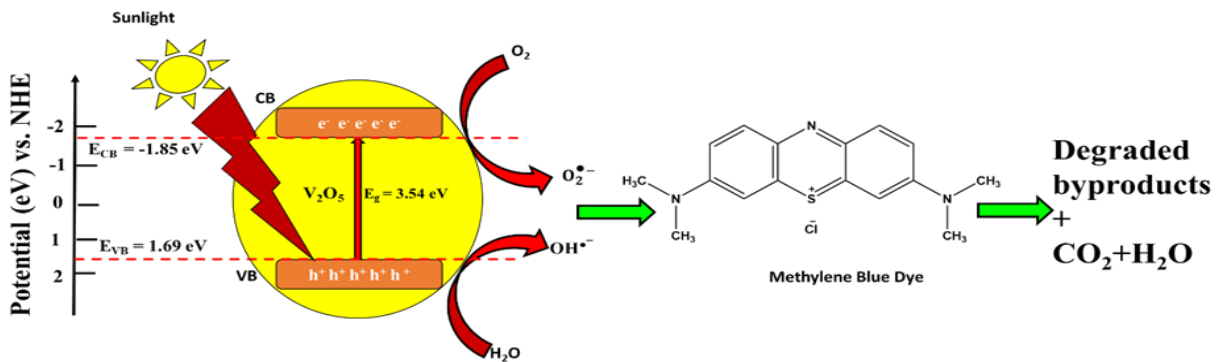
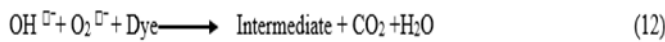
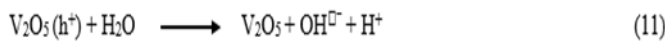
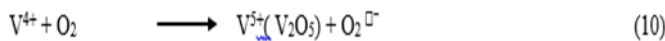
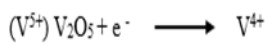
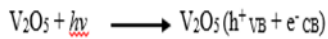


Fig. 10. Effect of scavenger on photocatalytic degradation of MB dye using pure V_2O_5 under sunlight irradiation.



Scheme 2. Schematic diagram of photocatalytic degradation of MB dye using pure V₂O₅.



The literature has described typical processes for the photodegradation of MB, and some degradation products and intermediates have been reported by GC-MS results. Ion chromatography was used to identify the formation of chloride, nitrate, and sulfate anions during the degradation of MB [48–50]. **Table 2** lists a few degradation intermediates that have been reported in the literature.

Table 2 lists a few degradation intermediates

Sl. No.	MB dye degradation intermediates	Mw
1.		303
2.		94
3.		136
4.		167
5.		230
6.		125

3.5.3 Stability

In general, the photocatalyst's stability significantly influences its practical applicability. After the MB dye was degraded, the prepared V_2O_5 photocatalyst's capacity for recycling was examined. After four uses, the photocatalyst still showed great efficiency (**Fig. 11a**). The synthesized V_2O_5 photocatalyst was found to have good cycling abilities. After the photocatalytic investigation, clarification of the structural stability of a photocatalyst was verified. The photocatalyst's XRD pattern (**Fig. 11b**) is identical before and after MB photodegradation. This demonstrated the V_2O_5 photocatalyst's structural stability. Additionally, the employed photocatalyst's morphology (**Fig. 11c**) matches that of the fresh photocatalyst. This also helped the V_2O_5 photocatalyst's morphological stability [51].

4. Conclusions

In summary, the effect of surfactant on structural and optical properties of V_2O_5 photocatalysts for degradation of MB was investigated. Surfactant addition caused the bandgap of the samples to broaden,

which resulted in the blue shift in the distinctive absorption peak of V_2O_5 nanocrystals. The average crystalline sizes of the pure V_2O_5 , V_2O_5 -SDS, V_2O_5 -TEOA, and V_2O_5 -Triton-X 100 nanocrystals were calculated to be around 22.71, 35.25, 36.33, and 42.71 nm, respectively. Pure V_2O_5 showed a reduction in PL intensity compared to surfactant assisted as prepared samples indicating that photo-induced electron-hole pairs are less able to recombine. The pure V_2O_5 nanocrystals had the highest photoactivity of 94.75% toward the degradation of MB dye due to their porous nature and small size confirmed by XRD. Further, the maximum electron-hole separation efficiency of the catalyst revealed the low PL intensity. The MB solution's photodegradation follows pseudo-first-order kinetics pure V_2O_5 shows a higher rate of photocatalytic degradation of MB than surfactant-assisted V_2O_5 . Pure V_2O_5 catalyst also showed high photostability and reusability, after 4-cycle tests. The scavenger study identified photogenerated holes (h^+) and superoxide radical anions ($O_2^{\cdot-}$) as the two major active species and proposed a possible photocatalytic degradation mechanism for MB dye degradation.

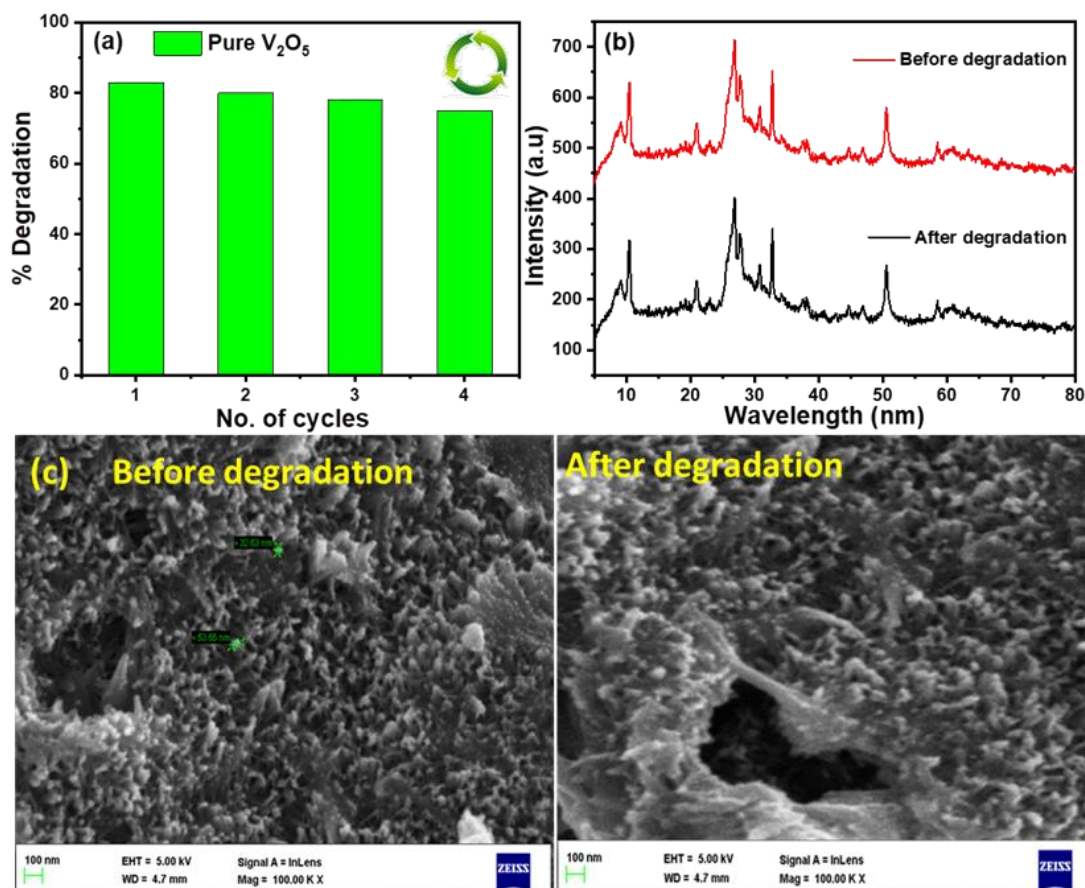


Fig. 11. (a) Photocatalytic degradation stability of pure V_2O_5 nanocrystals with MB dye. After five consecutive cycles, (b) the XRD pattern, and (c) SEM images of before and after degradation of V_2O_5 nanocrystals.

Acknowledgements

This work was supported by the Rani Channamma University and DST-SERB, Govt. of India. The authors are also grateful to the Indian Institute of Science (IISc), Bangalore for characterization support.

References

- [1] M. Balakrishnan, R. John, Iran. J. Catal. 10 (2020) 1–16.
- [2] A. Rostami-Vartooni, A. Moradi-Saadatmand, M. Bagherzadeh, M. Mahdavi, Iran. J. Catal. 9 (2019) 27–35.
- [3] S. Aghdasi, M. Shokri, Iran. J. Catal. 6 (2016) 481–487.
- [4] W.G. Menezes, D.M. Reis, T.M. Benedetti, M.M. Oliveira, J.F. Soares, R.M. Torresi, A.J.G. Zarbin, J. Colloid Interface Sci. 337 (2009) 586–593.
- [5] A. Ayub, Z.A. Raza, M.I. Majeed, M.R. Tariq, A. Irfan, Int. J. Biol. Macromol. 163 (2020) 603–617.
- [6] A. Ayub, K. Srithilat, I. Fatima, N.M. Panduro-Tenazoa, I. Ahmed, M.U. Akhtar, W. Shabbir, K. Ahmad, A. Muhammad, Environ. Sci. Pollut. Res. 43 (2022) 64312–64344.
- [7] Leili Shabani, Hamid Aliyan, Iran. J. Catal. 6 (2016) 221–228.
- [8] S.A. Mirsalari, A. Nezamzadeh-Ejhieh, A.R. Massah, Environ. Sci. Pollut. Res. 29 (2022) 33013–33032.
- [9] A. Norouzi, A. Nezamzadeh-Ejhieh, R. Fazaeli, Mater. Sci. Semicond. Process. 122 (2021) 105495–105507.
- [10] S.A. Mirsalari, A. Nezamzadeh-Ejhieh, A.R. Massah, Spectrochim. Acta - Part A Mol. Biomol. Spectrosc. 288 (2023) 122139–122149.
- [11] J.A. Arana-Trenado, D. Ramírez-Ortega, A. Serrano-Lázaro, A. Hernández-Gordillo, S.E. Rodil, M. Bizarro, Dalt. Trans. 51 (2022) 2413–2427.
- [12] A. Ayub, Z.A. Raza, Int. J. Biol. Macromol. 192 (2021) 1196–1216.
- [13] A. Ayub, A. Irfan, Z. Ali, R. Mazhar, Polym. Bull. 79 (2022) 807–827.
- [14] M.F. Sanakousar, V. C.C. V.M. Jiménez-Pérez, B.K. Jayanna, Mounesh, A.H. Shridhar, K. Prakash, J. Hazard. Mater. Adv. 2 (2021) 100004–100023.
- [15] D. Gogoi, P. Makkar, N.N. Ghosh, ACS Omega. 6 (2021) 4831–4841.
- [16] S.K. Jayaraj, P. Thangadurai, J. Mol. Liq. 319 (2020) 114368–114380.
- [17] F.M. Sanakousar, C. Vidyasagar, V.M. Jiménez-Pérez, K. Prakash, Mater. Sci. Semicond. Process. 140 (2022) 106390–106421.
- [18] M. Fauzi, F. Esmailzadeh, D. Mowla, N. Sahraeian, J. Mater. Sci. Mater. Electron. 32 (2021) 10473–10490.
- [19] N.M. Abd-Alghafour, N.M. Ahmed, Z. Hassan, M.A. Almessiere, J. Phys. Conf. Ser. 1083 (2018) 12036–12043.
- [20] M.F. Sanakousar, C.C. Vidyasagar, V.M. Jiménez-Pérez, N. Mounesh, A.H. Shridhar, React. Chem. Eng. 7 (2022) 1847–1872.
- [21] J. Pan, M. Li, Y. Luo, H. Wu, L. Zhong, Q. Wang, G. Li, Mater. Res. Bull. 74 (2016) 90–95.
- [22] S.K. Jayaraj, V. Sadishkumar, T. Arun, P. Thangadurai, Mater. Sci. Semicond. Process. 85 (2018) 122–133.
- [23] B. Das, M. Sharma, M.J. Baruah, B.P. Mounash, G. V. Karunakar, K.K. Bania, J. Environ. Chem. Eng. 8 (2020) 104268–104280.
- [24] D. Govindarajan, V. Uma Shankar, R. Gopalakrishnan, J. Mater. Sci. Mater. Electron. 30 (2019) 16142–16155.
- [25] M. Zebardast, A.F. Shojaei, K. Tabatabaieian, Iran. J. Catal. 8 (2018) 297–309.
- [26] S.D. Khairnar, M.R. Patil, V.S. Shrivastava, Iran. J. Catal. 8 (2018) 143–150.
- [27] F. Soleimani, A. Nezamzadeh-Ejhieh, J. Mater. Res. Technol. 9 (2020) 16237–16251.
- [28] A. Norouzi, A. Nezamzadeh-Ejhieh, Chem. Phys. Lett. 752 (2020) 137587–137597.
- [29] R.O. Yathisha, Y.A. Nayaka, C.C. Vidyasagar, Mater. Chem. Phys. 181 (2016) 167–175.
- [30] C.C. Vidyasagar, G. Hosamani, P. Kariyajanavar, R.O. Yathisha, Y. Arthoba Nayaka, Mater. Today Proc., 5 (2018) 22171–22180.
- [31] T.K. Le, M. Kang, S.W. Kim, Mater. Sci. Semicond. Process. 94 (2019) 15–21.
- [32] T.A. Abdullah, T. Juzsakova, R.T. Rasheed, A.D. Salman, M. Adelikhah, L.P. Cuong, I. Cretescu, Chem. J. Mold. 16 (2021) 102–111.

- [33] M.O. Chijioke-Okere, N.J. Okorochoa, B.N. Anukam, E.E. Oguzie, *Int. Lett. Chem. Phys. Astron.* 81 (2019) 18–26.
- [34] R.T. Rasheed, H.S. Mansoor, T.A. Abdullah, T. Juzsakova, N. Al-Jammal, A.D. Salman, R.R. Al-Shaikhly, P.C. Le, E. Domokos, T.A. Abdulla, *J. Therm. Anal. Calorim.* 145 (2021) 297–307.
- [35] S. Dianat, *Iran. J. Catal.* 8 (2018) 121–132.
- [36] H. Derikvandi, A. Nezamzadeh-Ejhieh, *J. Hazard. Mater.* 321 (2017) 629–638.
- [37] M. Rezaei, A. Nezamzadeh-Ejhieha, *Int. J. Hydrogen Energy.* 45 (2020) 24749–24764.
- [38] K.M. Shafeeq, V.P. Athira, C.H.R. Kishor, P.M. Aneesh, *Appl. Phys. A Mater. Sci. Process.* 126 (2020) 586–592.
- [39] S.A. Mirsalari, A. Nezamzadeh-Ejhieh, *Sep. Purif. Technol.* 250 (2020) 117235–117247.
- [40] S. Senobari, A. Nezamzadeh-Ejhieh, *J. Photochem. Photobiol. A Chem.* 394 (2020) 112455–112468.
- [41] A. Yousefi, A. Nezamzadeh-Ejhieh, *Iran. J. Catal.* 11 (2021) 247–259.
- [42] T.. S.. Suseno Ahmad Wijaya K, *Asian J. Chem.* 28 (2016) 347–350.
- [43] M.S. A.Suseno, K.Wijaya, W.Trisnuryanti, *Asian J. Chem.* 26 (2014) 70–73.
- [44] M. Mehrali-Afjani, A. Nezamzadeh-Ejhieh, H. Aghaei, *Chem. Phys. Lett.* 759 (2020) 137873–137882.
- [45] T. Senasu, K. Hemavibool, S. Nanan, *RSC Adv.* 8 (2018) 22592–22605.
- [46] N. Omrani, A. Nezamzadeh-Ejhieh, *Sep. Purif. Technol.* 235 (2020) 116228–116314.
- [47] M.M. Sajid, N.A. Shad, Y. Javed, S.B. Khan, Z. Zhang, N. Amin, H. Zhai, *Surfaces and Interfaces.* 19 (2020) 100502–100511.
- [48] A. Nezamzadeh-Ejhieh, M. Karimi-Shamsabadi, *Chem. Eng. J.* 228 (2013) 631–641.
- [49] A. Nezamzadeh-Ejhieh, S. Hushmandrad, *Appl. Catal. A Gen.* 388 (2010) 149–159.
- [50] A. Nezamzadeh-Ejhieh, M. Karimi-Shamsabadi, *Appl. Catal. A Gen.* 477 (2014) 83–92.
- [51] T. Chankhanittha, V. Somaudon, T. Photiwat, S. Youngme, K. Hemavibool, S. Nanan, *J. Phys. Chem. Solids.* 153 (2021) 109995–110015.